



UKAEA-CCFE-PR(25)357

W.Arter

Sensitivity Studies of Power Deposition Computed on Tokamak First Wall

Enquiries about copyright and reproduction should in the first instance be addressed to the UKAEA Publications Officer, Culham Science Centre, Building K1/0/83 Abingdon, Oxfordshire, OX14 3DB, UK. The United Kingdom Atomic Energy Authority is the copyright holder.
The contents of this document and all other UKAEA Preprints, Reports and Conference Papers are available to view online free at scientific-publications.ukaea.uk/

Sensitivity Studies of Power Deposition Computed on Tokamak First Wall

W.Arter

1

Sensitivity Studies of Power Deposition Computed on Tokamak First Wall

Wayne Arter, Senior Member, IEEE

Abstract—Profiles of power deposition on the first wall of the Joint European Torus (JET) tokamak experiment are fitted by tracing an analytic representation for the distribution of power from midplane along lines of magnetic field. The technique is used to help design plasma facing components (PFCs) in reactor-scale magnetic confinement devices, hence understanding how to employ it both efficiently and accurately is important. Focussing on JET divertor geometry, the work examines the sensitivity of the integrated power and maximum power per PFC tile to the representation of the magnetic field and to the discretisation of the tile's own geometry and that of other PFCs. For design it is helpful to reduce computation costs per realisation to a few seconds of elapsed time, and the work concludes with recommendations and guidelines for minimising cost whilst retaining adequate accuracy.

Index Terms—Tokamak, JET, uncertainty quantification, numerical sensitivity, plasma-facing components, power deposition

I. INTRODUCTION

Detailed motivation has been presented in the recently published [1] for the accurate simulation of the power deposited on the first wall of a tokamak due to leakage from the main plasma confinement region. There are three aspects to be considered to provide confidence in any simulation, namely verification, validation and uncertainty quantification (VVUQ). The recent [1] and other literature [2]–[4] give evidence for the adequacy of the SMARDDA modules in respect of the first two (VV) aspects. Specifically for the JET tokamak, unpublished reports from a multi-year campaign to speed execution of the software provide further VV. Extracted from this report material, the present work seeks to quantify uncertainty arising due to the discretisation of tokamak magnetic field and PFC surface geometry employed by the SMARDDA-PFC code. Such understanding ultimately enables accurate and efficient UQ of different field and geometrical designs.

The presence of plasma is key to the effect that the energy flux on first wall is expected to be directed parallel to the magnetic field, hence the power Q deposited per unit area can be reduced dramatically by arranging for grazing incidence of magnetic fieldlines on PFCs, with obvious benefits for reducing thermal stress. Observing that for a PFC tile of indicative extent $200 \, \mathrm{mm}$, a $1 \, \mathrm{mm}$ ripple equates to half a degree of normal deflection, it is a challenge to discretise field and geometry so that power deposition at angles of as little as 2^o or less can be economically calculated. This challenge forms the primary focus of the current work.

Wayne Arter is with the UK Atomic Energy Authority, Culham Science Centre, Abingdon, Oxfordshire OX14 3DB UK

The challenge is greater because the present strategy for triangulating geometry imported from a CAD package does not allow for adaptive mesh refinement, for example it is not possible to insert more triangles where gradients of power density Q are large. However, the surface mesher used, provided by the CADFIX TM package allows for a wide range of factors to influence triangulation, and locally written software enables systematic refinement of an initial mesh [3, Fig. 3].

The representation of the magnetic field **B** is by the *de facto* .eqdsk standard for an axisymmetric field in terms of poloidal magnetic flux function $\Psi(R,Z)$ and toroidal magnetic field component $B_T(\Psi)$ where (R, Z) are position coordinates in a vertical plane. The discretisation of B is all the more restricted since Ψ is specified as point values on a uniform rectangular grid. Previously published work on convergence has concerned relatively small areas of 'target' PFC, as little as one tile, where calculations of shadowing by immediately adjacent tiles can be made in a few seconds on a desktop for a detailed target with 50 000 triangles [3]. However, the JET divertor consists of approximately 600 tiles and reactor PFCs will have surface areas that are at least an order of magnitude larger still, thus the novelty and importance of the present work lies in enabling fast design job turnaround by use of coarser triangulations in configurations that allow more complex shadowing of one tile by another.

The next Section II describes the JET test cases in more detail, then Section III begins the presentation of results in a 'best case' situation to set the context, and largely disposes of the issue of magnetic field discretisation. The main study of sensitivity to surface meshing appears in Section IV, where many anomalies in the Q results become apparent. Their causes are identified, enabling the straightforward removal of most of them. Section V presents analysis that explains how the most awkward anomaly arises, then meshings which confirm the explanation, and show how the anomalies may be eliminated are presented in Section VI. The implications of the results are discussed in the concluding Section VII.

II. TEST CASE CONSTRUCTION

Calculations are given a runid as follows runid = eqid-gshad-gres

where *eqid* identifies the magnetic equilibrium, usually in terms of the last three digits of the JET shot number, and *gshad* and *gres* are respectively the roots of the .vtk filenames of the shadow and target or 'results' geometry triangulations respectively. Specification of the physics of the simulation is completed by giving the leakage power profile at midplane,

which is by default the formula due to Eich with parameters $\lambda_q = 0.017\,\mathrm{m}\ S = 0.0011\,\mathrm{m}$ and $P_{tot} = 10.2\,\mathrm{MW}$, mathematical details of which appear as [1, § A]. Other input parameters for SMARDDA-PFC, other than those which specify output diagnostics, serve to define the numerical algorithm. Sensitivities to most of the latter have been studied previously in ref [3], enabling the present work to focus on the discretisation of the magnetic field and of the geometry in the simulations.

A. Equilibria

For shot #89297 at $t=45.011\,\mathrm{s}$, the equilibrium was specified by two eqdsk files each with a different spacing for the samples of magnetic flux Ψ . These two solutions were produced with respectively a coarse 32×32 Ψ -mesh, and a much finer 256×256 Ψ -mesh. The former is given the simple eqid=297, the latter is referred to as fi297. The deposition profile for the shot is exponential decay [1, § III] with $\lambda_q=0.0066\,\mathrm{m}$ and $P_{tot}=10.5\,\mathrm{MW}$.

Since strike-point sweeping to spread the power deposition more widely over the PFCs might well be used in high power density discharges, a second shot is considered. The periodic sweeping is represented by a sequence of five equilibria equally spaced in time with the first and the last in the sequence at approximately the same phase, ie. sampling is at a interval $\tau_P/4$ where τ_P is sweep period. The flux-sweeping shot considered is JET #90271, where a $128 \times 128 \ \Psi$ -mesh is used throughout. Since more than one equilibrium is taken from this shot, they are numbered in time order after a decimal point, so that eqid=271.1 corresponds to the first equilibrium in the strike-point sweeping sequence at $t=49.0 \ s$, $t=49.0624 \ s$, $t=49.0624 \ s$, $t=49.0624 \ s$. For experimental details of these and related shots see [5].

B. Geometry

Since the original design of JET predates the universal employment of Computer Aided Design (CAD) systems, the acquisition and assembly of geometrical representations suitable for meshing required a deal of assistance as noted in the acknowledgements section at end. Fortunately the divertor design belongs to a later period where CAD files including construction details such as holes and fastenings were available. It followed that a workflow of modern relevance was possible for calculation of Q on the divertor, which is anyway a region of high interest to tokamak designers. The divertor consists of 24 repeats of a set of 24 tiles that spans 15° in toroidal angle, together with 48 repeats of a set of vertical plates joined (T5) to present their edges to the plasma.

The workflow begins by defeaturing the CAD description of the 15^o toroidal segment, removing irrelevant construction details, using the commercially provided CADFIX software. Attention focusses on the surface interfaces with vacuum, particularly the PFCs, which as the name implies are those directly facing the hot, centrally confined plasma, and especially on the narrow fillets illustrated in Figure 1. The retention of the latter demands the extra expense of locally fine mesh, thus two attempts were made to remove the fillets 'by hand'

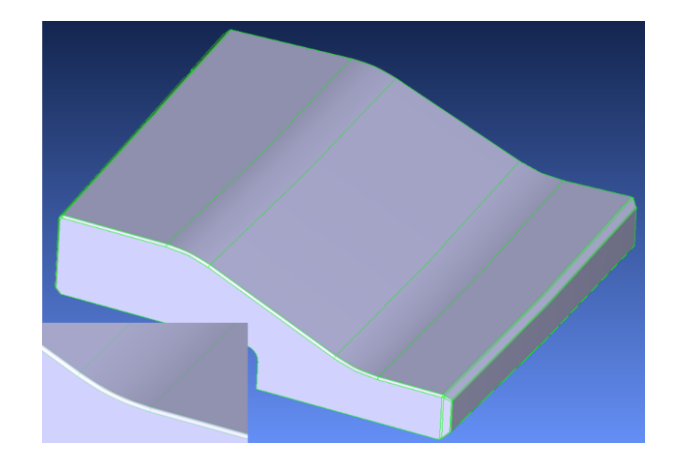


Fig. 1. JET divertor tile T6 design, illustrating fillet boundaries as pale green lines, closeup at bottom left.

as the automatic defeaturing facility was defeated by some of the three-way joins. Surface meshing of the defeatured CAD was also carried out using CADFIX, which has a GUI that allows for a wide range of different meshing strategies. Given that four defeatured representations (two with and two without fillets) of the CAD were available and two levels of automatic mesh refinement possible, this led to some 20-plus different meshes for the divertor repeat geometry, with a range of sizes of approximately 100 in terms of the total number of triangles N_{Δ} in the target. All the meshes were given labels traceable to a .vtk file keeping each one for future reference. The labels begin with 'c' if fillets have been removed and with 'd' or 'f' if retained, but as explained in Section A, the remainder of the label is an arbitrary string, excepting that a terminating '2' or '4' denotes respectively a refined or doubly-refined mesh (although not all automatically refined meshes are labelled in this way). Each separate meshing of a 15° segment is referred to as the 'a' model. The combination of three adjacent copies of the 'a' model is called the 'b' model, which therefore represents one octant (eighth) of the divertor. Replicating, translating and joining the 'a' model 24 times in toroidal angle gives the 'c' model and combining 'c' with meshes for other PFC geometry gives the full 360° 'd' model, see Figure 2, corresponding to the initial 15° 'a' mesh. Used as part of the geometry label, 'a-d' are prefixed by 'fs' and 'ft' to denote whether the file represents a shadow or target respectively. To save storage, instructions only are saved for re-generating the 'c' and 'd' models by SMARDDA code vtktfm.

III. PRELIMINARY STUDIES

A. Results for one Octant

Initial studies that included the JET limiters showed that little power was intercepted by them. Since the outer limiters are likely to be the most important PFC lacking rotational symmetry in their placement, when divertor power deposition is the main focus, it is reasonable to exploit the inherent symmetries of the divertor.

First, exploiting an eightfold symmetry, in order to verify the use of the software on a single JET octant, a series of

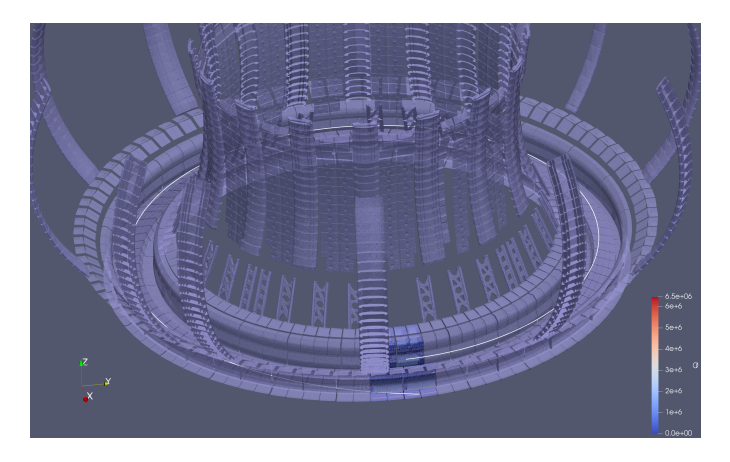


Fig. 2. 360° model for shadow viewed from outside looking down, with superimposed results for a 15° geometry providing an indicative fieldline, drawn in white.

calculations was conducted as indicated in Table I. As the table shows, these were used to test the adequacy of the meshing. It immediately makes clear that the total power deposited on the 15^{o} or $1/24^{th}$ segment of the divertor is approximately 400kW and therefore significantly lower than the value of $P_{tot}/24$ =425 kW expected given that total power in the midplane profile was $P_{tot} = 10.2 \,\mathrm{MW}$. It was then realised that $\lambda_q = 17 \,\mathrm{mm}$ was of order of one-third of the width of the SOL at midplane, so than only the first three efolds of the approximately exponential distribution of power could contribute to the total. Elementary integration of the decaying exponential reveals that this amounts to 95 % of the total, ie. $0.95 \times 425 \approx 404$ kW.

Following this renormalisation, Table I shows that the integrated power is accurately computed on the coarser mesh, and this level of accuracy extends even to total power on subsets of the geometry, see Figure 3. However it should be noted that in the first version of Table I, there was a maximum power for eqid=271.3 on the coarse mesh given as 7.261 MW, which was identified as spurious due to poor grid alignment (see Section V) and as there was only one offending triangle, the table entry was easily correctable. Compute times for a single processor desktop were of order a minute for the coarser grid and scaling approximately as N_{Δ} . (Multicore parallelism has been shown to bring wall-clock times down to 30 s for $N_{\Delta} = 10^6$.)

The segregation of the geometry indicated by Figure 3 is about the best that can be achieved using the SMARDDA software smanal which implements a clustering algorithm in poloidal angle, because seen from any point inside the PFCs, there is significant overlapping of at least two tile rows. Given that variation between the 15° segments is negligible, from the simple practical standpoint of reducing by a factor of three the work needed to segregate tile rows, further exploration was conducted using a 15° toroidal segment as target, although using a full 'd' model as the shadow.

A compact example of the plot of the power deposited on the divertor is provided by Figure 5, where it will be seen from T6 that shadowing leads to sharp cutoffs both in the toroidal direction (decreasing y in the figure) and the radial direction

Scan over strike-point sweeping of 45^{o} target geometries for GEOMETRY "CLE". "REFINED" DENOTES THAT BOTH TARGET AND Shadow mesh refined $\times 4$, thus columns 2 and 3 illustrate the SENSITIVITY TO MESH REFINEMENT.

Equil	Q_{max}	$\int Q/3$
-	MW/m ²	kW
271.1	6.884	407
Refined	6.735	405
271.2	5.380	399
Refined	5.412	403
271.3	5.002	400
Refined	5.046	400
271.4	5.326	399
Refined	5.380	400
271.5	6.947	407
Refined	6.735	405

The number of triangles for the 45^o target geometries were $N_{\Delta}=$ 182 367 and 729 468 respectively (60 789 and 243 156 in 15°), giving mean mesh sizes of respectively 6 mm and 3 mm. The shadow consisted only of the 360° divertor. Note that the integrated powers have been divided by three to compare with the 15° case studied later).

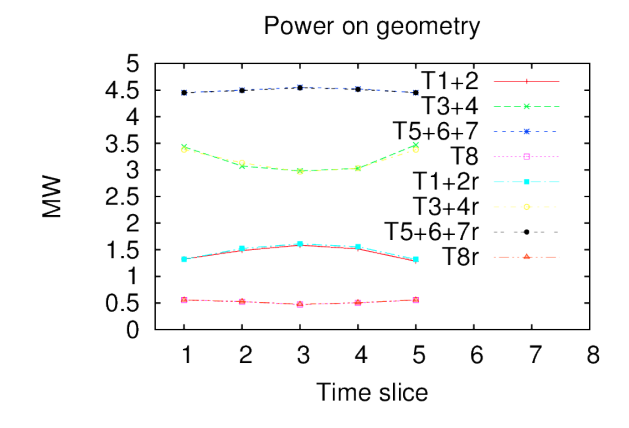


Fig. 3. Time history throughout strike-point sweep of power on different parts of the geometry. Labels finishing r denote results from refined calculations in Table I.

corresponding to increasing x. Despite this, good accuracy is achievable using relatively coarse meshes with sidelengths of order λ_q for recently explained reasons [1]. Since the coarse mesh of Table I has a side of mean length one-third of λ_a , a tenfold increase in execution speed is conceivable.

B. Effects of flux mesh size

Section II-A describes the equilibria labelled eqid=297 and eqid=fi297 as having size 32×32 and 256×256 meshes respectively. Figure 6 shows that their flux contour plots overlay very closely in the region of most interest for divertor power deposition, excepting what is confirmed to be a plotting issue at the X-point by inspection of the gradients of Ψ . At close to grazing incidence, Q depends sensitively on the angle between the field and the surface normal, but it does not depend greatly on the poloidal component of field, since this is much smaller than the toroidal component of 2 T. To be specific, the poloidal contribution needed to deflect B by one degree is approximately 0.04 T, whereas the entire poloidal field at the

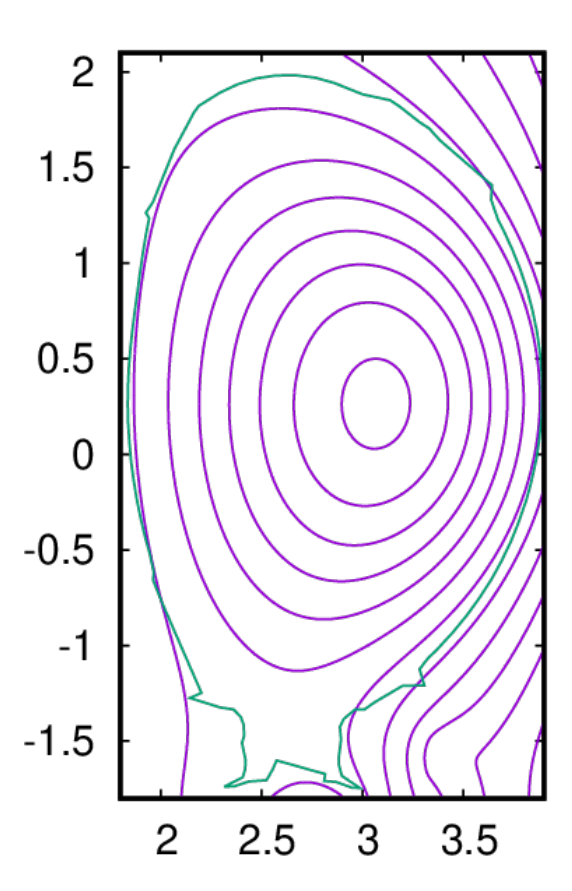


Fig. 4. Flux surfaces $\Psi(R,Z)$ for eqid=297, drawn in purple, superimposed on a profile or 'silhouette' of the JET first wall plotted in green. Distances are in metres.

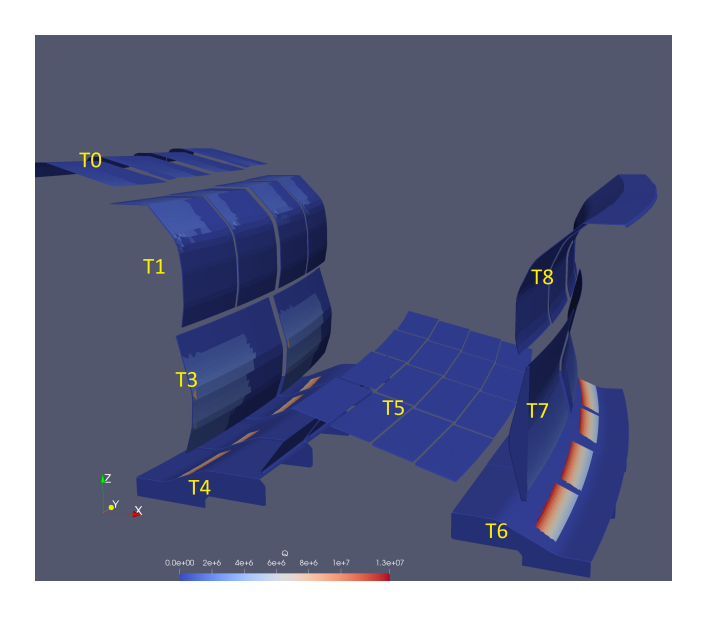


Fig. 5. Power deposition Q in MWm^{-2} for a 15^o toroidal segment of JET divertor, labelled with tile row numbers, for case $\it fi297$ - $\it fip-fiar$. The plasma is sited above the divertor geometry as indicated by Figure 4.

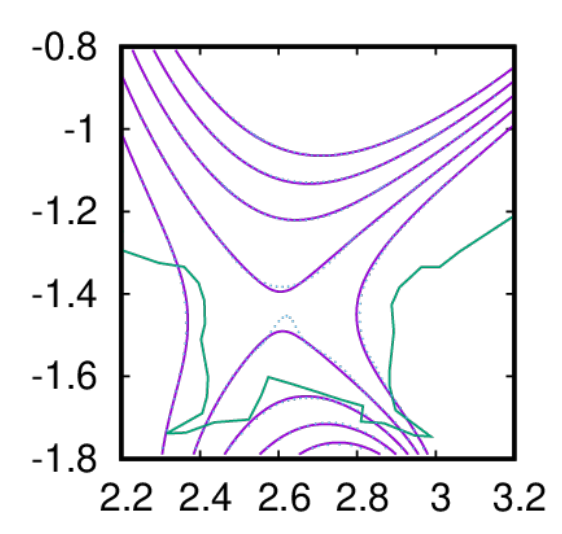


Fig. 6. Close-up of contour plots of flux $\Psi(R,Z)$ superimposed on JET silhouette (green), contour spacing 0.05. The equilibrium eqid=fi297 has contours drawn in purple, whereas those of the coarse mesh eqid=297 are shown as blue dots.

wall is approximately 0.2 T, thus Figure 6 suggests a negligible change in field direction from the different sampling.

In contrast, changes in the point value of Ψ feed into a formula involving an exponential. Error estimation begins by using the fact that the software outputs a quantity somewhat confusingly referred to as psista which is the value of Ψ at the midplane, ie. the computed end of the fieldline given a start-point on the PFC. Hence it is possible to plot the discrepancy in Ψ over the wetted area, as in Figure 7. Since $\Psi=\mathcal{O}(1)$, the discrepancy even on the coarse mesh, seems at first sight negligible, and indeed the shadow patterns are visually indistinguishable. but sadly the error of $|\Delta\Psi|\approx 2\times 10^{-3}$ implies that Q is in error by approximately $10\,\%$. However, the resulting error in Q on the fine mesh will be $0.1\,\%$ and easily tolerable.

The standard JET .eqdsk file contains a somewhat coarser $128 \times 128 \text{ } \Psi$ -mesh, so it is useful to understand the mechanism underlying the failure in flux conservation. For a randomly selected long fieldline, Figure 8 shows that it is not a consequence of inaccuracy in the Embedded Runge-Kutta (ERK) solver that computes the fieldline trajectories. Further investigation confirms the suggestion from Figure 6 that the error correlates with flux gradients. The system of fieldline equations solved for JET divertor models, advances positions in cylindrical polar coordinates by the corresponding components of axisymmetric equilibrium B. The finite-size mesh used to represent Ψ implies that the fieldline equations are solved subject to subgrid spatial uncertainty in the field. Generically, this deficiency leads to a failure of flux conservation, even when (pseudo-)time-step $\rightarrow 0$. This explanation is supported by the facts that the error is small and accumulates only over large spatial scales, but is worse the coarser the Ψ -mesh, and also greater where the flux gradients are larger.

The above arguments and simulations imply an empirical formula for the relative error in $Q=100\Delta\Psi_{num}$, where Ψ_{num} is the numerical value of Ψ in SI units, which is

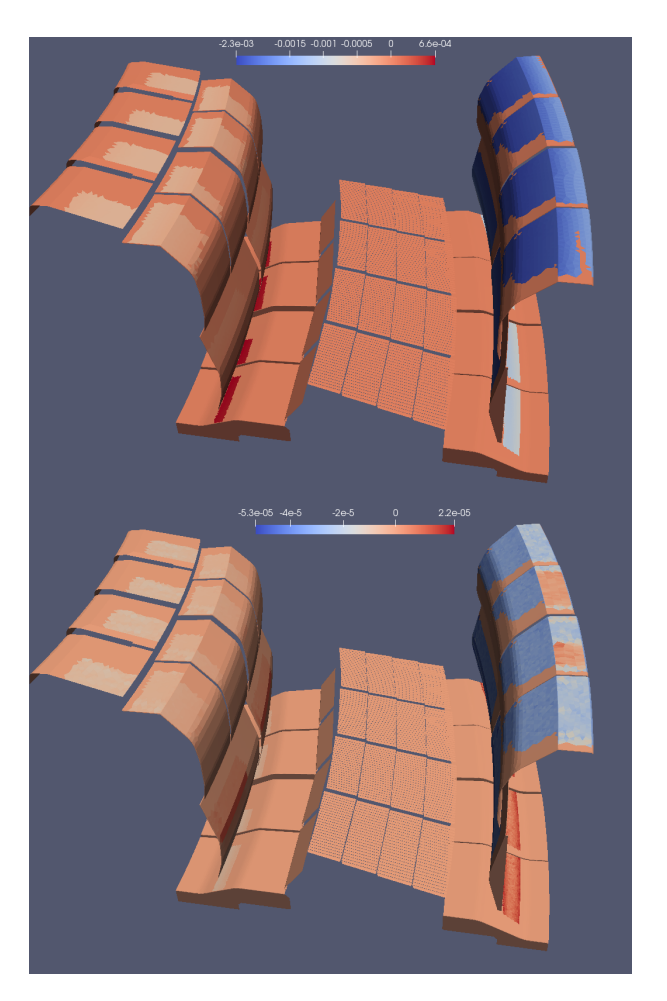


Fig. 7. Discrepant flux for powcal with 32×32 Ψ -mesh (top), $\max|\Delta\Psi|=2\times10^{-3}$ and 256×256 Ψ -mesh (below), smaller $\max|\Delta\Psi|=2\times10^{-5}$. eqid=(fi)297-fsdfip-fiar.

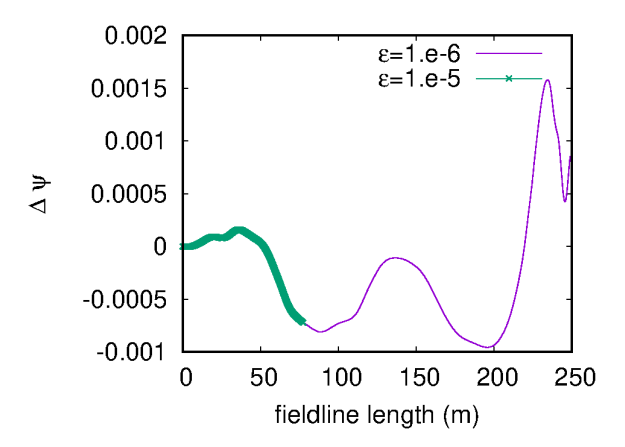


Fig. 8. eqid=297-fsdfip-fiar. Failure of magnetic flux conservation along fieldline 753 with 32×32 Ψ -mesh, diagnostic activated by uncommenting source code. ϵ is the tolerance used in the ERK solver. The fieldline computed with greater accuracy was allowed to continue beyond the inner midplane.

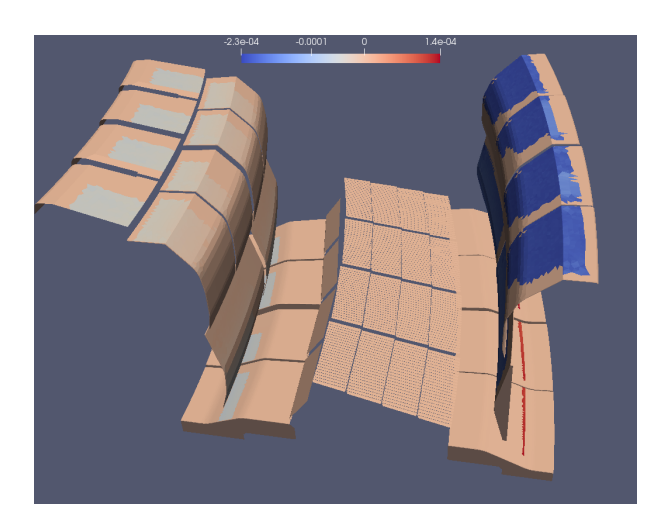


Fig. 9. Failure of flux conservation over divertor using the $128\times128~\Psi$ -mesh, $\max|\Delta\Psi|=2\times10^{-4}$. Equilibrium 271.1, #90271 at $t=49.0\,\mathrm{s}$.

confirmed by Figure 10, that indicates 2 % or less error. Hence the error is bearable for Q calculations using a 128×128 Ψ -mesh.

From the plot of flux contours in Figure 6, it is possible to estimate graphically that the spatial errors (in m) at the end point of the fieldline are $0.2\Delta\Psi_{num}$, equating to at most 0.04 mm for the 128×128 Ψ -mesh. Hence there is no visible effect on the extent of the inter-tile shadowing, since the triangle dimensions are typically at least several mm. The difference between flux values found at the two ends of a numerically computed fieldline is noted to be a powerful diagnostic of its accuracy.

IV. SENSITIVITY STUDIES

The otherwise trivial matter of labelling the 15° geometry segment by tile row and location, enables a workflow that is almost completely automatic for processing and analysing power deposition on each of 25 different gshad-gres combinations for a given eqid, in the notation of Section II. Thus the script that coordinates execution of the different modules geog, hdsgen and powcal needed to perform a SMARDDA-PFC simulation could in turn be invoked by a higher level script covering the 25 cases. A second script was written to invoke the smanal module for analysing powcal output to give maximum and integrated values of Q on each tile row, and to combine the results both in tabular and graphical form. Both equilibria jet271.1 and jet271.3 (subsequently abbreviated to 271.1 and 271.3 respectively) were analysed in this way. The combined plots were initially ordered by number of triangles in the target, later when it was realised that there was negligible power deposition on T5, plots were based on the total number of triangles representing the other tiles.

The results obtained by the automated process showed a number of anomalies. Firstly although the results for 271.1 and 271.3 tended to share the same features, those for *challmr-challmr2* and *challmr2-challmr2* differed. This was traced to the fact that the sorting algorithm, since the simulations shared the same size target, had reversed the order of analysis of their

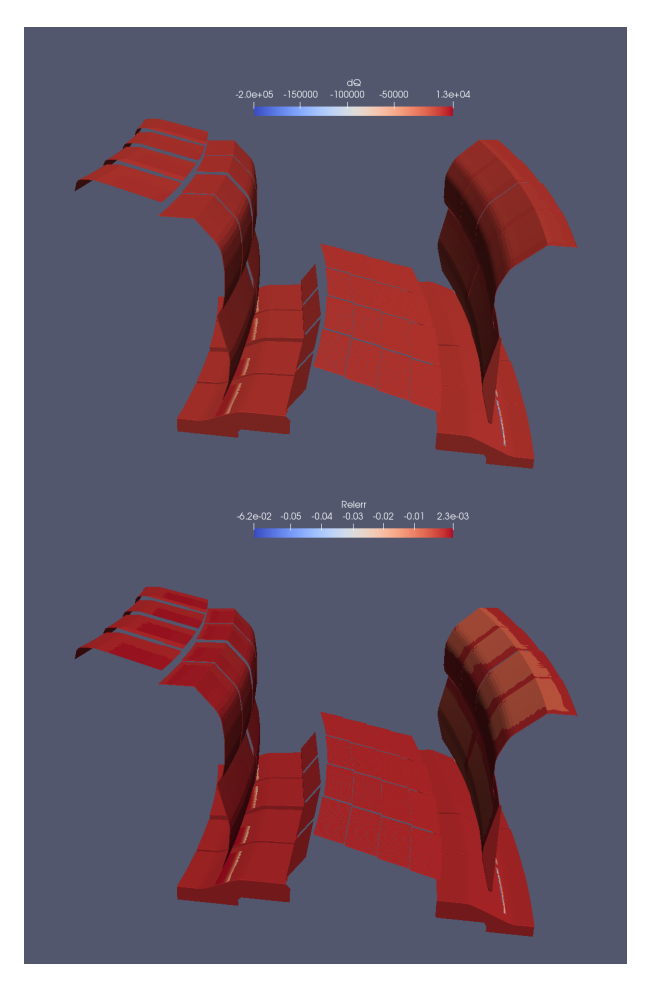


Fig. 10. Absolute (top) and relative error (below) in power deposition due to failure of flux conservation along a fieldline. *runid=271.1-fsdfia-fiar*.

output, and simply corrected. Simulations will henceforth, unless stated otherwise, be for 271.1 and so may be identified by the labels of their shadows and targets only (further omitting fsd and fta label prefixes). The second set of anomalies was confined to the T1 results and found to occur because a smaller area of the T1 surface had been meshed in simulations made before it was realised that notably in the flux sweeping calculations, power was deposited over much of T1 and indeed spread to T0. Depending on which T1 mesh was used, the total power deposited could change by a factor of approximately two. The simple fix made here was to omit T1 from the plotting and focus on the other tile rows.

Attention now transferred to the integrated and maximum powers on T6, which contains the region where the largest values of Q are expected in 271.1. Unexpected variability in their values was traced to inappropriate shadowing of the concave region on T6, as illustrated by Figure 11(a). Such a problem had been anticipated, and a control parameter ℓ_{crit} introduced so as to ignore fieldline intersections with surfaces when the length of fieldline was below this value. However, the critical length parameter was specified in units of the underlying uniform grid ('DDA' grid), partly for convenience of implementation, but also because it gives rise to a useful anisotropy in the metric. Spurious collisions may also occur

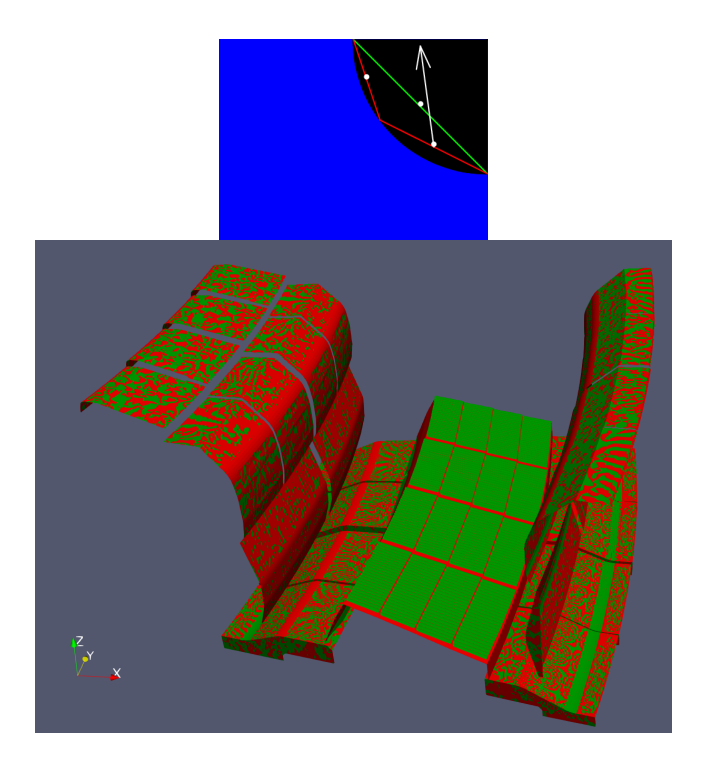


Fig. 11. (Top) Schematic of the spurious shadowing of a concave surface of the blue volume. The surface is represented by two elements in the finer meshing (red) and one surface in the coarser meshing (green). Fieldlines starting on the finer mesh soon intersect the coarse mesh. (Below) Overlay of meshes of the divertor geometry, clas and clar2. The first mesh is shown in green and the second, its refinement by a factor of four, in red.

with neighbouring triangles on the surface, in which case the length along the fieldline to intersection may be of order the triangle size, rather than the considerably smaller distance between two triangulations at the same point. Specifically, all calculations in the present section use a 'DDA' grid of size $16\,384\times65\,536\times16\,384$ to represent a volume of approximately $2\!\times\!20\!\times\!2$ m, so that eg. $\ell_{crit}=3$ corresponds to 0.4 mm in a radial direction, but over 0.9 mm in the toroidal (Y) direction.

Unfortunately, it seems that consequent on this choice of metric, premature fieldline termination took place over a significant area of T6 as indicated by Figure 11. leading to greatly reduced maximum and integrated Q on refined target meshes. Increasing ℓ_{crit} from 3 to 20 removed the effect for six of the visibly anomalous cases, and the remaining two, fias-fiar2 and challmr-challmr4, were fixed by use of $\ell_{crit}=50$. However, in the latter case, fieldline intersection with objects over 10 mm toroidally from the starting location will be ignored, which since the inter-tile separations range from approximately 5-14 mm means that other triangles on tile edges start to be incorrectly illuminated.

The remaining obvious anomalies are confined to the highest values of Q on different tiles, some of which are capable of affecting the global maximum. Inspection of the results using ParaView indicated that the anomalous global maxima were confined typically to a small number, often four or less of isolated triangles, which appeared to be spurious as a result of distortions to the T6 tile resulting from the defeaturing of the fillets, see Figure 12. However, all T6 results for the de-

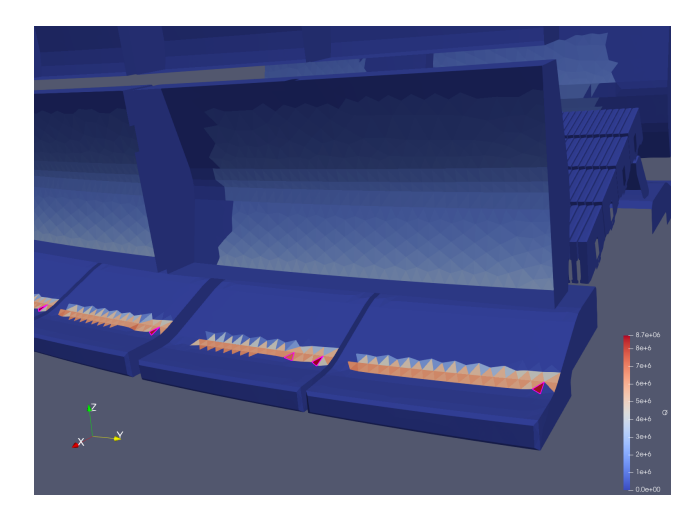


Fig. 12. Power deposition on T6, case fsdchasm-chasm, highlighted triangles have anomalously high values of Q

filleted tiles seemed to be affected to an extent. Anomalies in the T3 maximum are attributable to the field mis-aligned meshing described in Section V. Anomalous T1 maxima are linked to the effect discussed in the next Section VI, but in any event do not appear in the corrected plots that follow as Figures 13–14.

V. SURFACE ELEMENT PROPERTIES

For SMARDDA-PFC calculation of point Q, the key quantities are the barycentre of each triangle and its normal \mathbf{n} outward from the solid, which will here be assumed cylindrical with radius R. In the analysis, it is convenient to work in polar coordinates centred on the cylinder axis, see Figure 15 or Figure 17, so that

$$2R\sin\frac{\gamma}{2} = h_{\Delta}, \text{ so } h_{\Delta} \approx \gamma R$$
 (1)

in the limit of small h_{Δ}/R . Computation starts by writing down the Cartesian coordinates of each point ABCDE relative to an origin at the cylinder axis in the normal plane containing the midpoint of AB, thus

$$A,B: \qquad (0,R,\pm\ell)$$

$$C: \qquad (R\sin\gamma,R\cos\gamma,0)$$

$$D,E: \qquad (R\sin2\gamma,R\cos2\gamma,\pm\ell)$$
(2)

Triangles BCE and ACD share an unsatisfactory property, now discussed in detail for BCE in the Section V-A. Triangles ABC and CDE have very similar and overall satisfactory properties, shared with all the triangles considered in the Section V-B thereafter. There follows a study in Section V-C as to how small vertex displacements can lead to unsatisfactory triangle properties, and the importance of triangle alignment is summarised in Section V-D.

A. Problematic Surface Element

Elementary calculation gives the barycentre of BCE as

$$\frac{1}{3}(R[\sin\gamma + \sin 2\gamma], R[1 + \cos\gamma + \cos 2\gamma], 2\ell)$$
 (3)

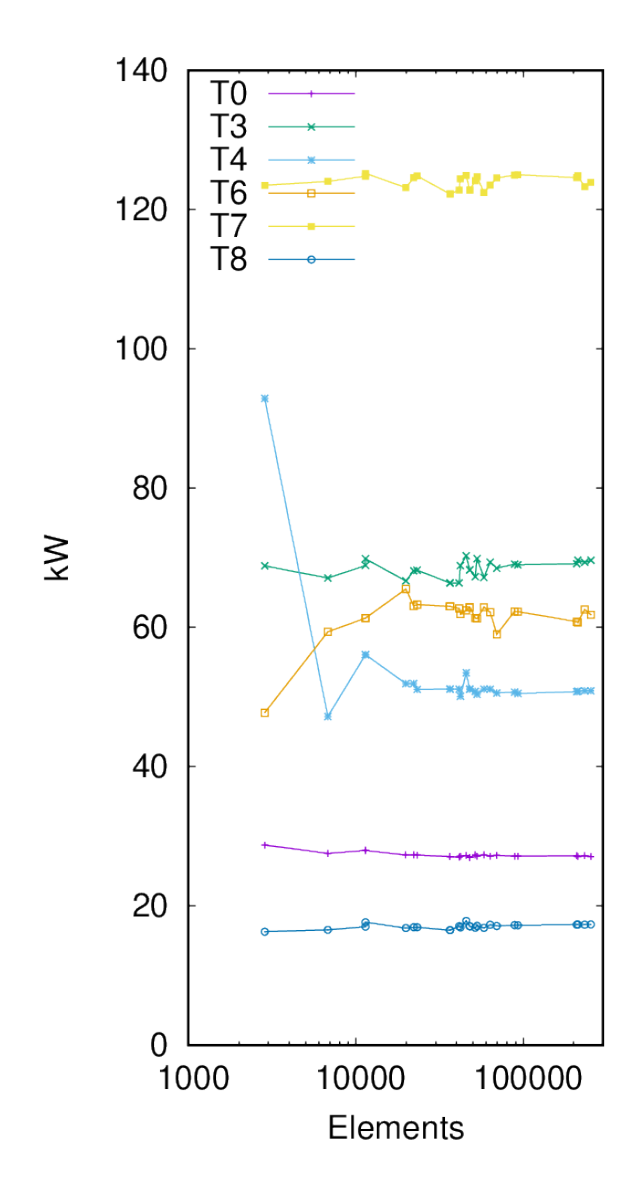


Fig. 13. Effects of mesh, broken down by tile row (15^o segment) . Total power (integrated Q) per row for each meshing, for eqid=271.1.

which corresponds to a polar angle β of

$$\tan \beta = \frac{\sin \gamma + \sin 2\gamma}{1 + \cos \gamma + \cos 2\gamma}, \text{ implying } \beta \approx \gamma$$
 (4)

in the limit of small h_{Δ}/R . The normal to the triangle BCE lies in the direction given by the vector cross product

$$(R\sin\gamma, R[\cos\gamma - 1], -\ell) \times (R\sin2\gamma, R[\cos2\gamma - 1], 0) = \ell R(1 - \cos2\gamma, \sin2\gamma, R/\ell \cdot 2\sin\gamma[\cos\gamma - 1])$$
 (5)

using the trigonometric identity $\sin \gamma(\cos 2\gamma - 1) - \sin 2\gamma(\cos \gamma - 1) = 2\sin \gamma(\cos \gamma - 1)$, so that the normal is directed in polar angle η_{θ} , where

$$\tan \eta_{\theta} = \frac{1 - \cos 2\gamma}{\sin 2\gamma}, \text{ so } \eta_{\theta} \approx \gamma$$
 (6)

which accurately corresponds to the normal to the cylinder surface at the barycentre angle β . However, the normal has a

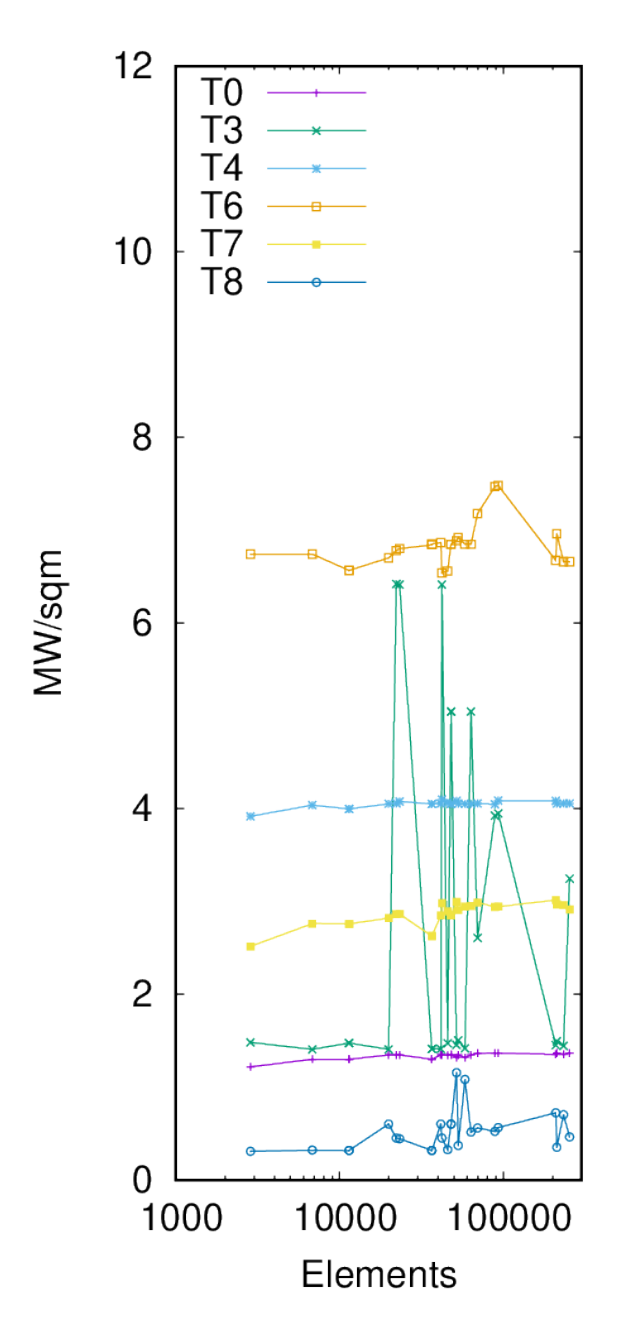


Fig. 14. Effects of mesh, broken down by tile row (15 o segment). Maximum Q per row for each meshing, for eqid=271.1.

component in the z direction, so is tilted out of the vertical by an angle η_z given by

$$\tan \eta_z = \frac{R}{\ell} \cdot \frac{\sin \gamma (\cos \gamma - 1)}{\sqrt{2 - 2\cos 2\gamma}}, \text{ so } |\eta_z| \approx \frac{R}{\ell} \frac{\gamma^3/2}{2\gamma} = \frac{R}{\ell} \frac{\gamma^2}{4}$$

in the limit of small h_{Δ}/R .

1) Mean Value Theorem: It is worth noting that triangles BCE and ACD are counter-examples to the possibility of a fully 2-D application of the mean value theorem (MVT). In one dimension, meaning application to a scalar function y of a single variable x, the MVT is the result that the secant must be parallel to a continuously differentiable curve for at least one point lying on the curve between the ends of

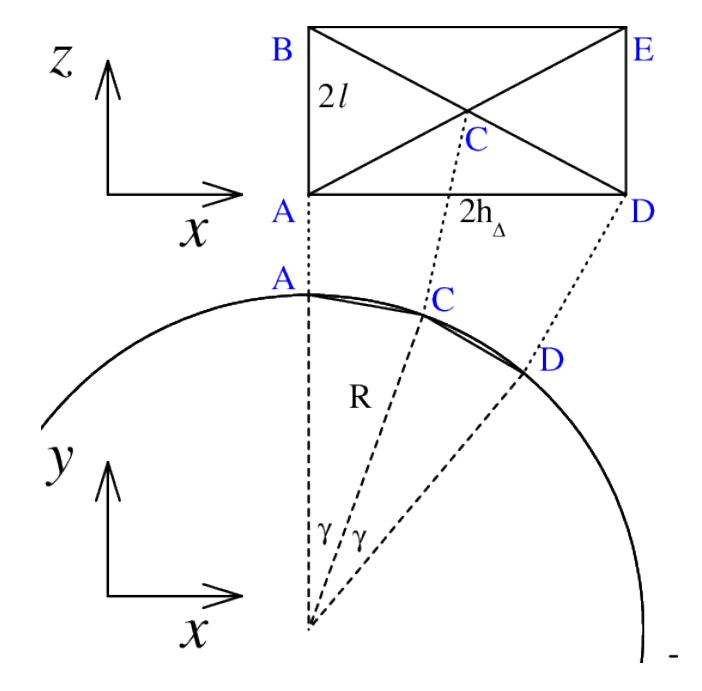


Fig. 15. Schematic of triangulation of cylinder of radius R. The triangle ABC has base 2ℓ and height h_{Δ} , where 'height' corresponds to an angle γ subtended at the cylinder axis. Conversely, triangle BCE has base $2h_{\Delta}$ and height ℓ .

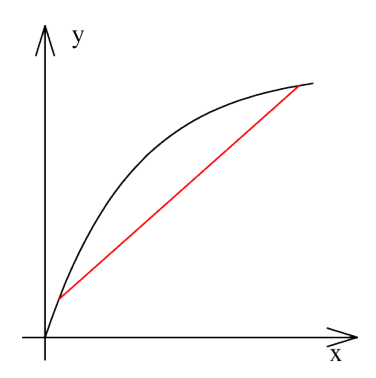


Fig. 16. The mean value theorem in 1-D. At a value of x between the ends of the secant (shown in red), the curve y(x) has the same gradient dy/dx as the scant

secant, as graphed in Figure 16. It follows immediately that the normal to the secant must coincide with the normal at such a point, giving cause to hope that there might be at least one surface point close to a triangle with vertices on the surface, that has a common normal direction. However, all points on the curved surface of a cylinder with axis parallel to z have normal directions in the xy-plane, whereas it was just shown that BCE and ACD have normals with a z-component, thus the MVT cannot apply as hoped.

B. Satisfactory Surface Elements

In Figure 17, the points are

$$A, B: \qquad (0, R, \pm \ell)$$

$$C, C': \qquad (R \sin \gamma, R \cos \gamma, \pm \ell)$$

$$D, E: \qquad (R \sin 2\gamma, R \cos 2\gamma, \pm \ell)$$
(8)

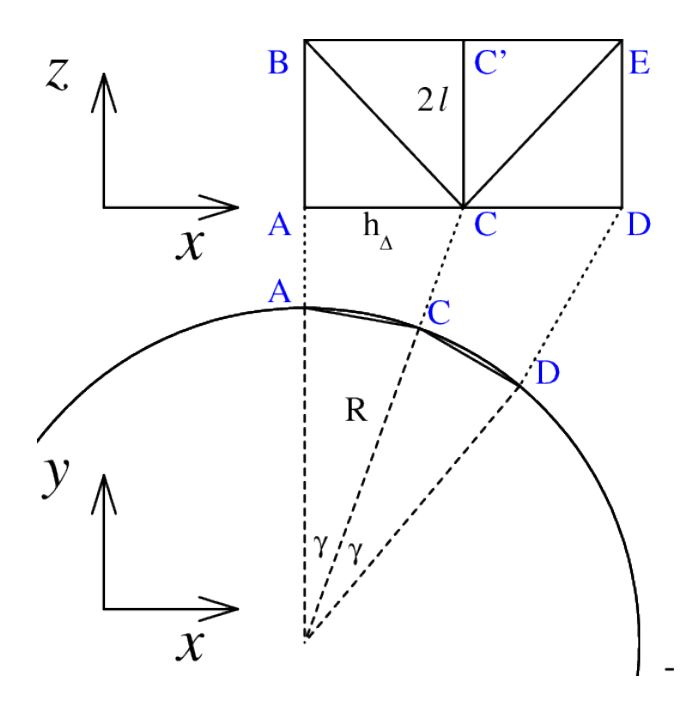


Fig. 17. Schematic of second triangulation of cylinder of radius R. All the triangles ABC, BCC', CC'E and CDE have base 2ℓ and height h_{Δ} , where 'height' corresponds to an angle γ subtended at the cylinder axis.

Analysis proceeds as in Section V-A. The barycentre of ABC is

$$\frac{1}{3}(R\sin\gamma, R[2+\cos\gamma], -2\ell) \tag{9}$$

which corresponds to a polar angle β of

$$\tan \beta = \frac{\sin \gamma}{2 + \cos \gamma}, \text{ or } \beta \approx \gamma/3$$
(10)

in the limit of small h_{Δ}/R . The normal to the triangle ABC lies in the direction given by the vector cross product

$$(0,0,2\ell) \times (R\sin\gamma, R[\cos\gamma - 1], -2\ell) = 2\ell R(1 - \cos\gamma, \sin\gamma, 0)$$
(11)

so that the normal is directed in polar angle η , where

$$\tan \eta = \frac{1 - \cos \gamma}{\sin \gamma}$$
, so $\eta \approx \gamma/2$ (12)

This normal is obviously inconsistent with radial direction $\gamma/3$ at barycentre, but it is nonetheless accurate to the extent of lying within the range of directions spanned by the triangle. Symmetry implies that the other triangles in Figure 17 have the same properties, for example CDE has barycentre at angle $5\gamma/3$ and the normal directed at $3\gamma/2$ without a z-component. In the context of a conical rather than cylindrical surface, the 'Union Jack' meshing was criticised for having this property [3, Sec. II-C], but this criticism has now to be seen as misplaced. The advantage compared to the case of Section V-A, that the normal has no spurious z-component, outweighs the inconsistency between location and value.

C. Misaligned Surface Element

In this example, it is supposed that point B is slightly displaced in x through an angle δ , so that

$$A: \qquad (0, R, -\ell)$$

$$B: \qquad (R\sin\delta, R\cos\delta, \ell)$$

$$C, C': \qquad (R\sin\gamma, R\cos\gamma, \pm \ell)$$
(13)

Analysis proceeds as in Section V-A. The barycentre of ABC is clearly only slightly displaced by an angle of order δ from $\gamma/3$ in the limit of small h_{Δ}/R . The normal to the triangle ABC lies in the direction given by the vector cross product

$$(R\sin\delta, R[1-\cos\gamma], 2\ell) \times (R[\sin\delta - \sin\gamma], R[\cos\delta - \cos\gamma], \ell) = \ell R(2\cos\gamma - \cos\delta - 1, 2\sin\gamma - \sin\delta, R/\ell \cdot [\sin\delta(1-\cos\gamma) + \sin\gamma(\cos\delta - 1)])$$
(14)

so that the normal is directed in polar angle $\eta_{\theta} \approx \frac{1}{2}(\gamma + \delta/2)$, but as δ increases from zero, there will be a significant z-component inclined at angle

$$\eta_z \approx \frac{R}{\ell} \frac{\gamma \delta}{2} (\gamma - \delta)$$
(15)

scaling linearly while $|\delta| \ll \gamma$ with the size of the misalignment.

D. Importance of Surface Element Alignments

The results of the proceeding subsections have shown how if no side of a triangle sides lies parallel to z, then its normal has a spurious z-component. This is important if the z-direction corresponds locally to the largest component of the magnetic field B, which in a tokamak is the toroidal direction ϕ , for then the spurious contribution $B_{\phi}n_{\phi}$ may be comparable to the true contributions. Figure 18 shows speckled behaviour of the Q-profile, following from the fact that $Q \propto \mathbf{B}.\mathbf{n}$ may differ significantly from triangle to adjacent triangle when the triangle edges are not well aligned to the magnetic field direction thanks to changes in the $B_{\phi}n_{\phi}$ contribution. However, provided at least one edge of a triangle lies approximately in the toroidal direction (y in the figure), then the Q point values are more accurate. The effect of misalignment on the quadrature is much reduced since the spurious contributions tend to cancel, eg. in Figure 15 ACD and BCE have precisely opposite normals, so any spurious contribution will be limited by the change in B over the separation of their barycentres.

VI. ADDITIONAL SENSITIVITY STUDIES

Drawing on the above experience, the CAD description of T4 and T6 was defeatured for a third time, retaining the fillets. Meshings of the new geometry were combined with meshings of T0, T1, T3, T7 and T8 to produce .vtk files for the divertor 'repeat', and another 11 cases were constructed.

Although for most SMARDDA-PFC fieldline-tracing calculations, the default size of ℓ_{crit} is adequate, a more reliable way to avoid problems might be to shadow the target with an identical mesh. This was not initially considered

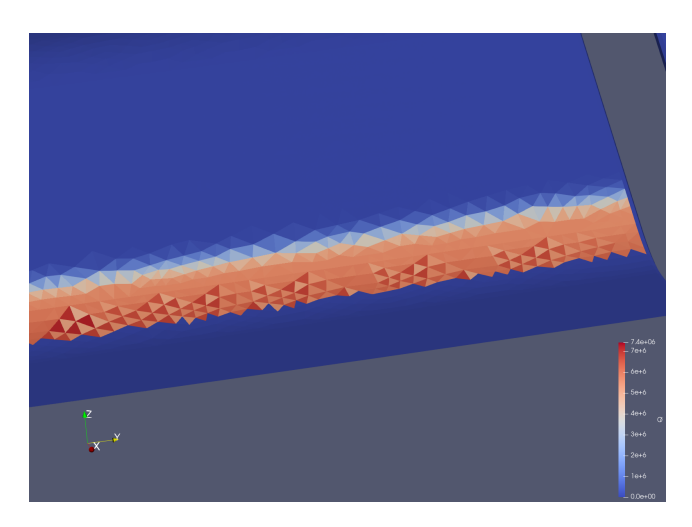


Fig. 18. Power deposition on T6, case *fsdfitt3-fitt3*, showing 'speckling' in some of the regions near the boundary of high-Q deposition.

because previously studied tokamak geometries had all had discrete toroidal symmetries whence SMARDDA-PFC could impose periodic boundary conditions to reduce the problemsize to the geometry 'repeat', ie. by one-twelfth in MAST-U application [3]. The shadow geometry had thus to have the same meshing in every repeat. However, the JET results of Section IV confirm SMARDDA-PFC capability to treat multi-million triangulations, hence inhomogeneous shadowing to be feasible. The preceding experience indicates that the shadowing geometry needs to be as fine as the target geometry 'locally'. The meaning of locally in this context was explored by using 360° divertor shadow meshes generated as shown in Figure 19. Replacing only the target geometry with a fine mesh is shown to be vulnerable to spurious deposition when edges of convex tiling are exposed as shown in Figure 20, indicating that adjacent 'local' repeats should also be meshed finely for robustness.

The meaning of locally in the context of accurate shadowing will depend on precise details of geometry, but a common situation will be a configuration involving rows of rectangular tiles, with approximate sizes $L_{\phi} \times L_{\theta}$ where L_{ϕ} and L_{θ} are the dimension in the toroidal and poloidal directions respectively. Supposing shadowing by tiles on other rows to be less critical than by tiles of the same row, then coarser meshing might be allowed once a path following a fieldline has moved a poloidal distance of L_{θ} , equating to a poloidal angle of $\Delta \theta = L_{\theta}/r$, where r is the minor radius. Assuming the local fieldline safety factor is q, the corresponding toroidal angle is $q\Delta\theta$, equating to a distance travelled of approximately $qR\Delta\theta$. Supposing each tile to subtend a toroidal angle of approximately L_{ϕ}/R , the number of additional fine copies of a tile needed by the shadow geometry at each side of the target is thus

$$N_{f\pm} = \frac{qL_{\theta}R}{L_{\phi}r} \tag{16}$$

Evidently if the target consists of n_T copies of the tile in a row of interest, then the total number of fine copies needed

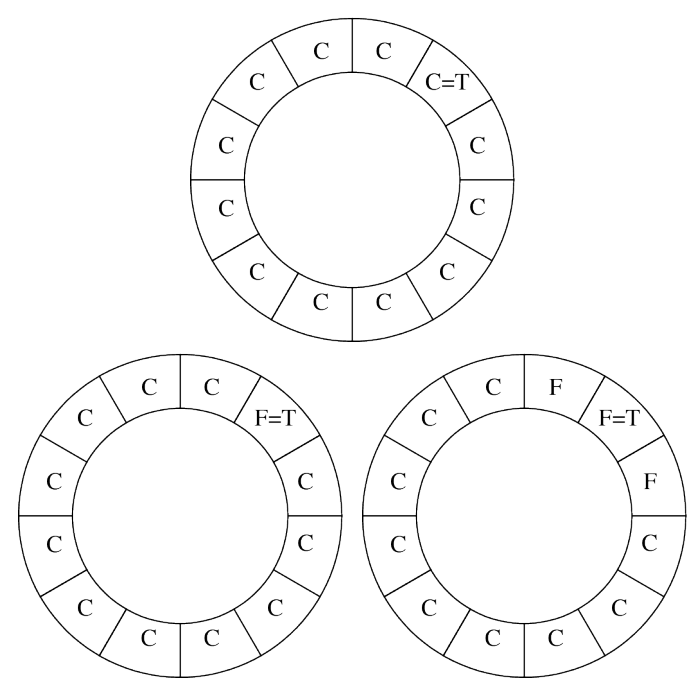


Fig. 19. Schematics of toroidally 360° shadowing geometry, imagined viewed from above. '=T' here denotes the location of the target segment. At the top is the original periodic arrangement of repeats with the coarse (C) meshing. Inhomogeneous shadows are sketched underneath: the left one shows a fine mesh (F) coinciding with the target, whereas the right shows the target bracketed by fine meshes. (Note that a more accurate schematic of the JET meshes would have 24 segments rather than the twelve drawn above.)

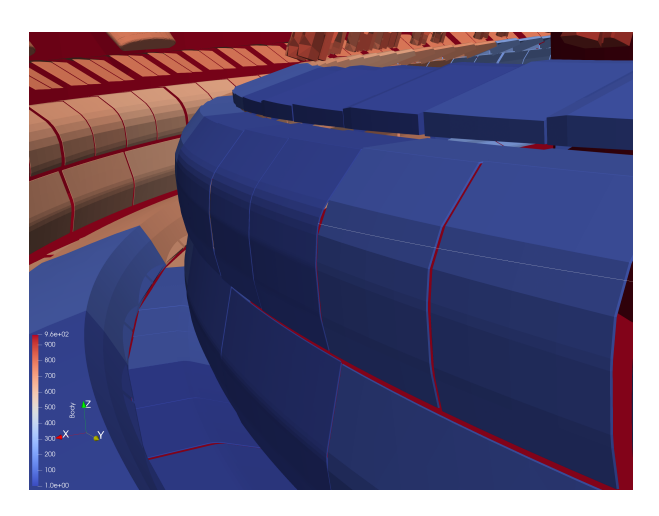


Fig. 20. Exploratory case *filp4-dint4* with inhomogeneous shadow, showing fieldline incorrectly missing adjacent coarsely-meshed convex tile geometry.

by the shadow is

$$N_f = 1 + 2 \left[\frac{qL_{\theta}R}{n_T L_{\phi}r} \right]^+ \tag{17}$$

where $[\cdot]^+$ denotes that the bracketed quantity should be rounded up to the nearest whole number.

The new 11 cases, all with fillets, were run semiautomatically as described in Section IV for 271.1. The results are shown in Figures 21–22 which now show an absence of major anomalies, with again the coarser grids producing results very little different from those obtained with up to a hundred

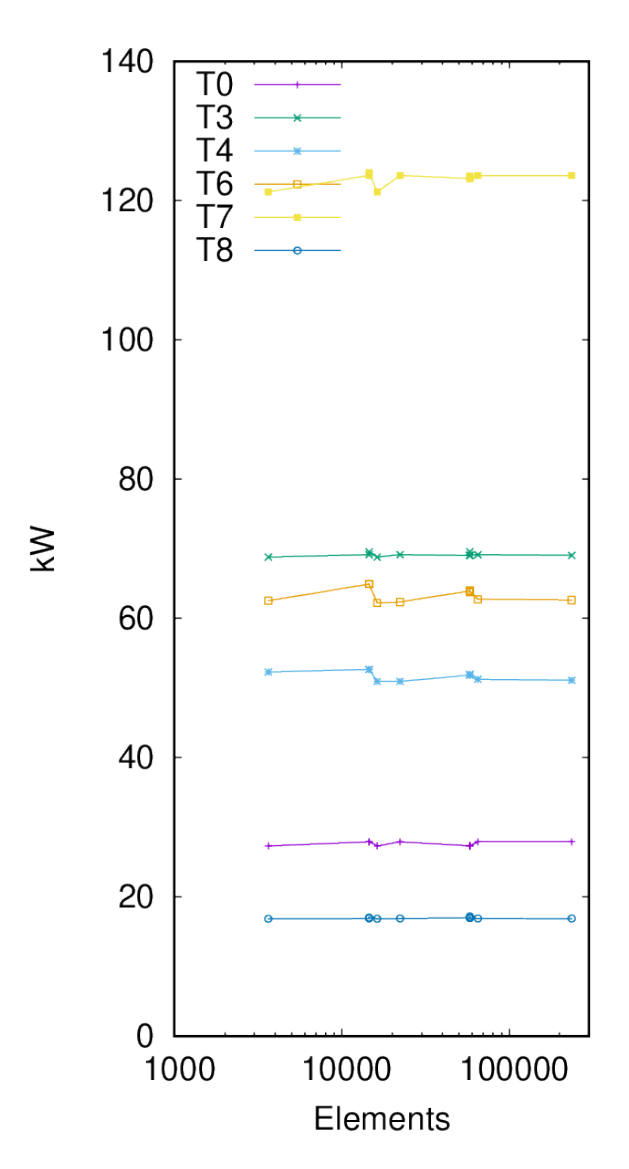


Fig. 21. Effects of mesh, broken down by tile row (15^o segment) . Total power (integrated Q) per row for each meshing, for eqid=271.1.

times more triangles (and therefore given that computational cost is approximately proportional to N_{Δ} , up to a hundred times more expensive). The most significant variation is in Q_{max} on T6, but inspection shows that the higher values are all associated with a curvature sensitive meshing of T6 and its successive refinement. The *fitt-ditt* meshes responsible, although arguably a more accurate representation of the surfaces than the others, are misaligned, accounting for the anomaly in Q_{max} .

VII. CONCLUSION

The work presented here in Section IV, Section V and Section VI has shown that it is possible to compute power deposition in the divertor to an accuracy better than $10\,\%$ and probably exceeding that of the physical model, with a remarkably small number of target triangles and a relatively coarse mesh for the flux function. The achievement is assisted by the relatively simple pattern of power deposition in the

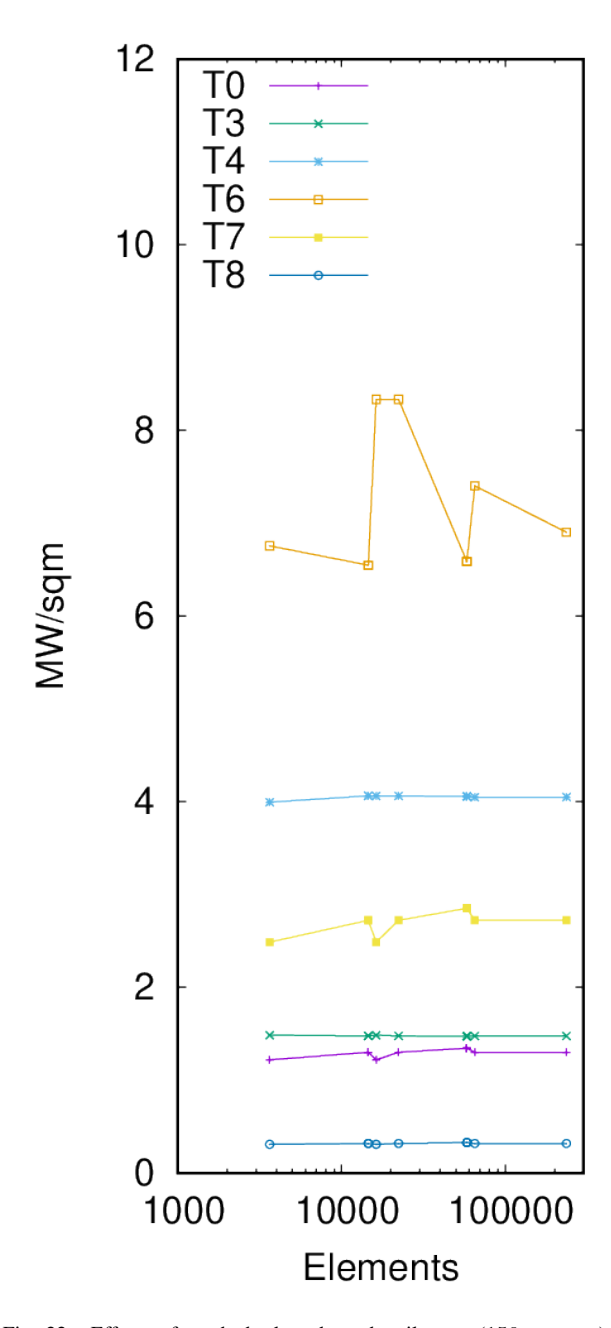


Fig. 22. Effects of mesh, broken down by tile row $(15^o$ segment). Maximum Q per row for each meshing, for eqid=271.1.

divertor. Unfortunately Sections IV- VI have also shown that it is quite possible to have comparable or worse errors with much finer geometry and flux function discretisations.

The following guidelines are proposed based on the current work and the companion paper [1].

- Great care should taken in defeaturing CAD, especially when the plasma facing surfaces might be affected. It may be safer, albeit slower, to rebuild surfaces using specially selected curves and face geometry extracted from the CAD database.
- 2) Make an initial coarse mesh of the main plasma facing surfaces with triangles of side no greater than the typical lengthscale of input power profile, viz. λ_q in the case of

- a simple exponentially decaying profile. Check results using a $4\times$ refined meshing. Certain critical areas, normally tile or limiter edges adjacent to the main surfaces, may require much finer meshing, down to assembly tolerance of typically a millimetre, and in the absence of special indication, all such areas should be gridded to a finer length scale.
- 3) Meshing should be aligned with the main direction of the magnetic field, viz. one side of each triangle should be aligned with or close to the toroidal direction in a tokamak.
- 4) Where shadowing and target geometry coincide, they should share a common triangulation. In cases where results are needed only over a fraction of the toroidal angle, coarser triangulation of more distant shadow features is acceptable, based on the formula of Section VI.

There is an important practical point that execution speed may be significantly increased by inserting into the shadow geometry 'cutouts' and 'beancans', non-physical surfaces that intercept fieldlines certain *not* to connect with the midplane, and 'skylights', non-physical surfaces certain to connect to the midplane. These additions may greatly reduce the total length of fieldline that is followed, easily outweighing the costs of the relatively minor increase in size of the shadow geometry.

ACKNOWLEDGEMENT

I thank students Dominic Calleja and Ted Stokes for their contributions to the UQ and meshing aspects of this work respectively. Paul Carman and Martin Kocan provided important information, including CAD files, about the JET PFCs. Gabor Szepesi and Nick Hawkes provided .eqdsk files. Special thanks are due to Scott Silburn for the profile data and much advice besides. This work has been carried out within the framework of the EUROfusion Consortium, funded by the European Union via the Euratom Research and Training Programme (Grant Agreement No 101052200 – EUROfusion) and from the EPSRC[grant number EP/W006839/1]. To obtain further information on the data and models underlying this paper please contact PublicationsManager@ukaea.uk. Views and opinions expressed are however those of the author(s) only and do not necessarily reflect those of the European Union or the European Commission. Neither the European Union nor the European Commission can be held responsible for them.

REFERENCES

- [1] W. Arter, "Error Estimation for Plasma Power Deposition in Tokamak First Wall Designs," *IEEE Transactions on Plasma Science*, vol. XX, no. XX, p. XX, 2024, https://dx.doi.org/10.1109/TPS.2024.3399929.
- [2] W. Arter, E. Surrey, and D. King, "The SMARDDA Approach to Ray-Tracing and Particle Tracking," *IEEE Transactions on Plasma Science*, vol. 43, no. 9, pp. 3323–3331, 2015, http://dx.doi.org/10.1109/TPS.2015. 2458897.
- [3] W. Arter, V. Riccardo, and G. Fishpool, "A CAD-Based Tool for Calculating Power Deposition on Tokamak Plasma-Facing Components," *IEEE Transactions on Plasma Science*, vol. 42, no. 7, pp. 1932–1942, 2014, http://dx.doi.org/10.1109/TPS.2014.2320904.
- [4] W. Arter, G. Fishpool, D. King, H. Leggate, V. Riccardo, and E. Surrey, "Modelling of tokamak plasma interaction with engineered surfaces," in 14th World Congress on Computational Mechanics (WCCM) ECCOMAS Congress 2020, online video 2021, 2021, https://slideslive.com/38943983.

[5] S. Silburn, G. Matthews, C. Challis, D. Frigione, J. Graves, M. Mantsinen, E. Belonohy, J. Hobirk, D. Iglesias, D. Keeling *et al.*, "Mitigation of divertor heat loads by strike point sweeping in high power JET discharges," *Physica Scripta*, vol. 2017, no. T170, p. 014040, 2017.

APPENDIX

A. MESHES

For the meshing of the JET divertor geometries, use was made exclusively of the CADFIX mesher. This allows meshing strategies that may insert points into surfaces, to satisfy the Delaunay (empty triangle circumcircle) property, or try to account for surface curvature, the latter giving the option to increase element size on flatter surfaces by setting suitable control parameters. Other parameters set the maximum and minimum acceptable lengths for mesh edges, the extreme values of acceptable angles in the triangulation and the maximum and minimum number of divisions allowed along an edge &c., together with further parameters that set the relative importance of satisfying the preceding constraint parameters. This parameter space was freely explored for five different CAD descriptions over several years, in such a way as to defeat a systematic naming convention, hence the arbitrary choice of mesh label, beyond the choice of beginning with 'c' if fillets have been removed and with 'd' or 'f' if retained in the CAD prior to meshing.

The problem with describing any meshing is not only the sheer number of parameters that may affect the result, but also the difficulty that even small changes to an algorithm, as minor as changing the order of processing a CAD part, may make significant changes to the result. The decision whether to join point P1 to P2 or P1 to P3, has to be taken on the basis of comparison of real numbers, which may be very close to coincidence if there is symmetry in the local geometry, and thus the decision effectively be made at random. Since the first marginal choice may thereafter affect all subsequent mesh connectivity, there is no expectation that meshing will be reproducible from one software release to another, or even from one computer architecture to another. Hence the only reliable way to achieve reproducibility is to retain the mesh files as described in the main text, files which may then be inspected using 3-D viewing software such as ParaView should it be necessary to check details of the triangulations. The number of triangles N_{Δ} in each description of the geometry is however recorded herein, as it gives an approximate value for the average mesh length $h_{\Delta} = \sqrt{A_{\Delta}/(2N_{\Delta})}$. Since the total area A_{Δ} is here approximately a square metre, $N_{\Delta} = 20\,000$ corresponds to $h_{\Delta} = 5 \, \mathrm{mm}$. Triangle numbers are presented in Table A. Note that in some cases (calculations) the shadow mesh of the 15° cell differs from the target by the insertion of cut-outs, skylights, etc. and so has a label differing by one character, typically an 'r' or 't' is replaced by 's'.

TABLE II MESHED GEOMETRIES, ORDERED IN TERMS OF TOTAL NUMBER OF TRIANGLES IN THE MESH, FOLLOWING THE SUBTRACTION OF THE NUMBER OF TRIANGLES IN T5.

Label	Triangles	Label	Triangles
challmr	2851	clet204	51635
dint	3631	clar	52963
challma	6792	dint4	58096
challmr2	11404	filt204	58206
dint2	14524	fiar	63375
ditt	16236	ditt3	64944
cfallmm	19883	challnm	69469
challn	22159	challn2	88636
ditt2	22248	chasm2	92868
chasm	23217	clet2042	208492
ftavm	36486	clar2	211852
fsazm	41405	filt2042	232824
chatm	42084	ditt4	235728
challmr4	45616	fiar2	253500
ftaum	47871		